



# Investigation of the effect of light scattering on transmitted laser intensity at the weld interface during laser transmission welding of 3D printed thermoplastic parts

Le Anh-Duc<sup>1</sup> · Benoît Cosson<sup>1</sup> · André Chateau Akué Asséko<sup>1</sup>

Received: 8 June 2023 / Accepted: 12 September 2023 / Published online: 6 October 2023  
© The Author(s), under exclusive licence to Springer-Verlag France SAS, part of Springer Nature 2023

## Abstract

3D printing has offered cost-effective, lightweight, and complex parts. To extend their applications, 3D printed parts need to be welded in order to form the larger functional assemblies. For this purpose, Laser Transmission Welding (LTW) is a promising joining technology. This paper aims to investigate the light scattering effect on the intensity profile of the laser heat source during the transmission through the 3D printed laser-transparent part. Indeed, the inherent design of the 3D printing technology results in a complex heterogeneous microstructure with a significant amount of porosity inside the printed parts. Such structure induces the optical diffusion (i.e. light scattering) of the laser beam within the 3D printed parts. This phenomenon leads to the reduction of the transmitted energy arriving at the weld interface, which directly influences the quality of the joint and its mechanical performance. The approach adopted in this paper is to propose a ray-tracing model to simulate the optical paths of the laser beam through the 3D printed laser-transparent part, which is able to evaluate changes in the laser heat source at the weld interface directly linked with the light scattering effect within the microstructure of the parts. Experimental measurements are performed to assess the transmitted intensity flux distribution using an image processing technique, instrumented with a digital camera and macro lens. The numerical results show good accordance with the experimental one, which proves the confidence of the proposed ray-tracing model. Finally, 3D transient thermal model of the LTW process is performed using the FEM software COMSOL Multiphysics® to confirm the influence of the scattering effect on the temperature field and thus on the quality of the weld.

**Keywords** Laser transmission welding · 3D printing · Light scattering · Ray-tracing simulation · Thermoplastic polymers · Weld interface · Transmitted laser intensity

## Introduction

Fused Filament Fabrication (FFF) based 3D printing of continuous carbon fiber reinforced composites (CCFRCs) has demonstrated impressive capabilities in reproducing

Benoît Cosson and André Chateau Akué Asséko contributed equally to this work.

✉ Benoît Cosson  
benoit.cosson@imt-nord-europe.fr

Le Anh-Duc  
anh-duc.le@imt-nord-europe.fr

André Chateau Akué Asséko  
andre.akue.asseko@imt-nord-europe.fr

<sup>1</sup> IMT Nord Europe, Institut Mines Télécom, Univ. Lille, Centre of Materials and Processes, Villeneuve d'Ascq F-59653, France

complex shapes, delivering superior mechanical properties, and creating lightweight structures [1–3]. Despite its potential benefits, due to the inherent design of layer-by-layer production, the mechanical performances of the 3D printed of CCFRCs remain limited by the orientation of the fibers in the printing plane, and the relatively low strength of inter-layer bonding [4–6]. This drawback becomes particularly problematic when dealing with complex mechanical loads in a three-dimensional context. One way to address this technological challenge is to utilize a hybrid approach that combines two different processes: 3D printing and Laser Transmission Welding (LTW). This method involves 3D printing of anisotropic CCFRCs components in different printing directions, then using LTW to join the parts together. This hybrid method allows for the production of objects in which the continuous reinforcing fibers are arranged to provide support for multi-directional mechanical loads.

As carbon fibers absorb most of the energy from the laser, CCFRCs components are absorbent to the incident laser radiation. Transparent filler material was used for LTW of CCFRC components in [7]. The two joining components are held together by a clamping device, while the transparent filler material and the joining partners are kept together only by the elastic force of the polymeric monofilament. The radiation passes through the transparent filler material and is absorbed by the two joining components. The produced heat is transferred to the filler material via heat conduction. All three components melt, and once the materials cool down, they fuse permanently together through the diffusion of polymer molecules.

An alternative approach for the assembly process is to produce small thermoplastic windows (100% pure), which are either transparent or semi-transparent to the laser radiation, while 3D printing one of the components to be joined. These windows enable the laser radiation to pass through the transparent component and be absorbed by the absorbent composite component at the interface. As a result, this localized heating causes the thermoplastic to melt, creating a strong bond at the weld interface.

Achieving a high-quality weld requires careful control of the interface weld temperature. This temperature is affected by multiple factors, including the optical and thermal properties of the components being welded, as well as the specific parameters used during the LTW process [8–10]. As the laser beam propagates through a heterogeneous medium, like a 3D printed component that contains a substantial amount of voids, it gets reflected and refracted every time it encounters an air-matrix interface. This occurrence results in laser beam scattering, which decreases the amount of transmitted energy reaching the weld interface [11]. As a consequence, the joint's quality and mechanical performance are directly impacted [12–15]. Kuklik et al. [16] used 3D printing and LTW process parameters to predict the weld seam strength by using a neural network-based expert system with an accuracy of 88.1%.

It has been demonstrated that the transmissivity and scattering behavior of thermoplastic 3D printed components are a function of 3D printing process parameters [17]. In this study, we aim to comprehensively investigate the impact of light scattering on the intensity profile of the laser heat source during its transmission through a 3D printed laser-transparent part. We propose a ray-tracing model to simulate the optical paths of a laser beam through a 3D printed laser-transparent part. By using the proposed model, it is possible to predict the changes in the laser heat source distribution at the weld interface, which are directly linked to the light scattering effect within the microstructure of the parts.

The methodology employed in this study builds upon our previous work [12, 18–20]. However, the novelty of this paper lies in the specific case study: the application to

3D printed thermoplastic parts. This investigation comprises the following key aspects: First, we conduct microstructural characterization of the 3D printed thermoplastic parts by varying the printing parameters; The second step involves generating numerical microstructures that represent the void shapes and porosity of the materials; In the third step, we evaluate the influence of microstructural differences and sample thickness on the resulting intensity profiles of the laser at the interface. This evaluation is achieved through a quantitative numerical/experimental comparison; Finally, we examine the effect of light scattering on the interface temperature, and consequently, on the weld quality. By addressing these aspects, we present a comprehensive analysis of laser transmission through 3D printed parts. This analysis provides crucial insights for optimizing the welding process, enhancing weld quality, and improving the final product's mechanical properties.

As a first step, the microstructures of the samples printed under different printing parameters will be examined by means of optical microscopy. According to the microstructure analysis, the numerical RVEs of the samples will be generated. Subsequently, ray-tracing simulations will be performed to model the diffusion patterns of the light transmitting through the samples. Then, the transmitted intensity flux distributions of the laser beam will be generated at the weld interface and compared for different samples. In order to validate the numerical model, an image processing technique equipped with a digital camera and macro lens will be used to perform experimental measurements that assess the transmitted intensity flux distribution at the weld interface. Finally, 3D transient thermal model of the LTW process will be conducted using the FEM software COMSOL Multiphysics®. The thermal model will allow for confirming the influence of the scattering effect on the temperature field during the LTW process. Accordingly, the quality of the weld can be predicted.

## Experimental section

### Materials and processing

The transparent Poly-Ethylene Terephthalate Glycol-modified (PETG) filament, with a diameter of 1.75 mm, supplied by Polymaker™ was used as the feedstock in this study. As indicated in the datasheet, the material has a density of 1.25 g.cm<sup>-3</sup> and a glass transition temperature of 81°C. The nozzle temperature is recommended in the range of (230 – 260°C). A Composer Desktop 3D - printer from Anisoprint™ was used to print all the samples. Aura™ software was used to slice 3D CAD models and assign the FDM processing parameters, as summarized in Table 1. The CAD models used to manufacture the samples have a rectangular

**Table 1** FDM processing parameters used in this study

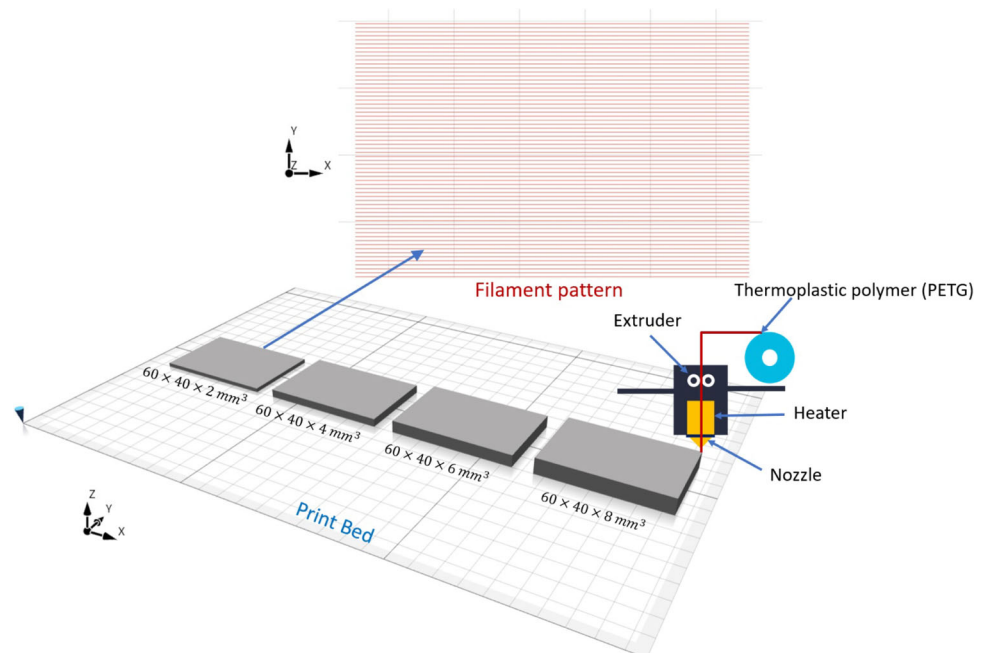
Processing parameter	Value
Nozzle temperature ( $^{\circ}\text{C}$ )	240
Nozzle diameter ( $\text{mm}$ )	0.4
Bed temperature ( $^{\circ}\text{C}$ )	75
Print speed ( $\text{mm/s}$ )	30
Layer thickness ( $\text{mm}$ )	0.2, 0.3
Infill pattern	line
Infill percentage (%)	100
Extrusion multiplier	1

bar shape, with rectangular plan dimensions of  $L = 60\text{mm} \times W = 40\text{mm}$ , with different thicknesses as depicted in Fig. 1. The nozzle temperature was set to  $T_n = 240^{\circ}\text{C}$ . Apart from the parameters in Table 1, all other printing parameters were fixed, but the layer thickness was varied between 0.2mm and 0.3mm.

### Sample microstructures investigation

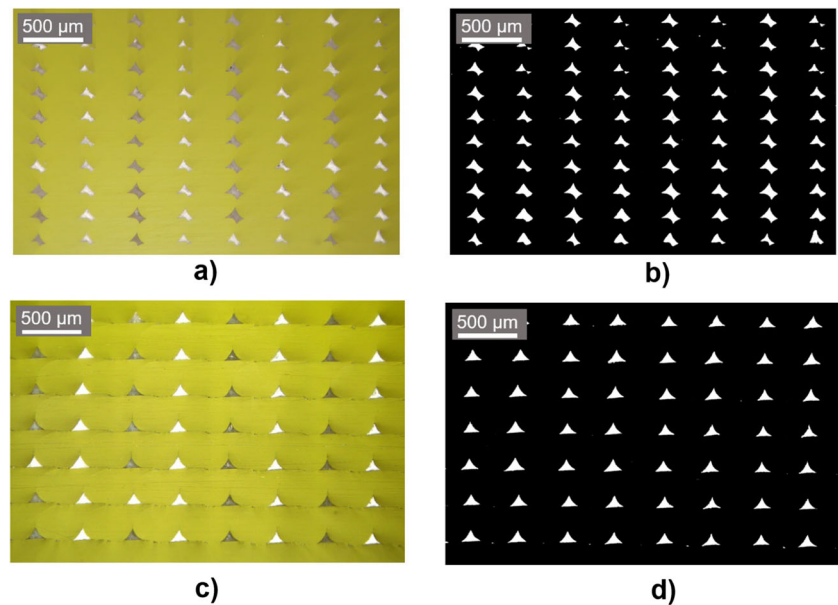
Optical microscopy of the sample cross-sections was conducted to investigate void content and void morphology. To prepare for microscopy, the samples were cut with a saw in the middle, in a way that filaments were perpendicular to the cut plane. The samples were then ground with SiC sandpaper up to a maximum grit size of 1200 (Struers Inc., Cleveland, OH, USA). Finally, the sample surfaces were polished using diamond colloidal suspension to a final grit size of  $1\mu\text{m}$ .

**Fig. 1** 3D printing of thermoplastic samples with different thicknesses



Optical microscopy was carried out by means of a ZEISS Axio Zoom.V16 digital microscope and DeltaPix InSight™ V6.7.4 software. Figure 2 shows the void morphology of two sample types I and II, which were printed under two levels of the layer thickness ( $e = 0.2\text{mm}$  and  $e = 0.3\text{mm}$ ) respectively. The shape of voids changes from a predominantly fully astroid-shaped for sample type I ( $e = 0.2\text{mm}$ ) (Fig. 2a) to half astroid-shaped for sample type II ( $e = 0.3\text{mm}$ ) (Fig. 2c). These voids were formed by the gaps between the filaments deposited during printing and were actually grooves aligned in the direction of the filaments. Although the nozzle used to extrude the molten material is circular (i.e.  $D = 0.4\text{mm}$ ), during deposition, the filament was pressed down to a smaller layer thickness (i.e.  $e = 0.2\text{mm}$  and  $e = 0.3\text{mm}$ ) and became elliptical. As can be seen in Fig. 2, in both cases, the bottom surfaces of the filaments cooled down quickly to form round edges. On the contrary, the top surfaces of the filaments were relatively flat due to the interaction between the nozzle and the molten polymer, and the extrusion pressure during the printing process [2]. For the layer thickness of 0.3mm, because of a large amount of extruded material, the extrusion pressure is more important, which pushes the material to the side. Moreover, a higher amount of molten polymer carries more thermal energy, resulting in better rheological properties. Therefore, the top surfaces flatten. For the layer thickness of 0.2mm, the top surfaces of the filaments are slightly deformed due to these circumstances but still maintain relatively round edges. These deformed edges, then, together with the bottom surfaces of the subsequently deposited filaments, form mostly astroid-shaped voids.

**Fig. 2** Void morphology of the 3D printed parts and image analysis procedure to find the void fraction. (a) Unprocessed optical image (Sample type I); (b) post-processed image (Sample type I); (c) Unprocessed optical image (Sample type II); (d) post-processed image (Sample type II)



The printing parameters shown in Table 1 were chosen in order to obtain these two typical void morphology of the 3D printed parts. Numerous studies have reported the internal structure of the FDM parts to be similar to the structure depicted Fig. 2 [1, 21–23]. Different printing parameters than those used in this study might be needed for other machines/materials to achieve the same microstructures.

The void area fraction was measured by post-processing cross-section optical images of the samples in ImageJ software. For each treatment condition, five images were analyzed from different cross-section images to find the average value of the porosity. The voids can be distinguished from the matrix by performing an image segmentation based on pixel classification. As shown in Fig. 2a and c, the green part signifies the matrix. The porosity of the sample can be calculated based on the void area fraction over the area of the whole image as shown in Fig. 2b and d. These results will then be used to generate the numerical micro-structures of the samples in the flowing section.

### Laser intensity profile measurement

The aim of the experimental measurements is first, to obtain the initial intensity flux distribution of the laser beam without considering the light scattering effect and second, to characterize the intensity flux distribution at the weld interface considering the light scattering effect during the transmission through the 3D printed laser-transparent part. The measurement method used in this study was reported in our previous work [18]. To prepare for the experiments, sample surfaces were ground using SiC sandpaper up to a maximum grit size of 1200 (Struers Inc., Cleveland, OH, USA) and then polished using a diamond colloidal suspension up to a final grit

size of  $1\mu\text{m}$ . The experimental set-up can be shown in Fig. 3, which is maintained in a darkroom to eliminate any external light that may be parasitic and affect the captured images. The idea is to capture the spot of the laser beam on the back side of the sample using a digital camera (i.e. Canon EOS 5D) equipped with a macro lens (i.e. Canon EF 100mm  $f/2.8$  USM Macro). Three images with different exposure levels (i.e. under exposure, normal exposure, and over exposure) are needed to build a master curve for the calibration of the grayscale according to the levels of light energy (as depicted in Fig. 4). To do so, the camera is set to manual mode in order to impose the same settings, except the exposure time for all samples (i.e. Bracketing exposure setting mode as can be shown in Fig. 5). Further explanations about the calibration procedure can be found in Ref. [18]. One master curve can be built for each sample, however, these curves are expected to be identical for all samples. To minimize the impact of noise and errors, an average master curve is used for the calibration of all images, which is shown in Fig. 6.

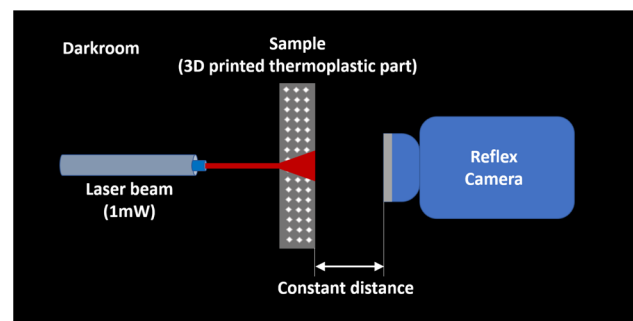


**Fig. 3** Experimental set-up

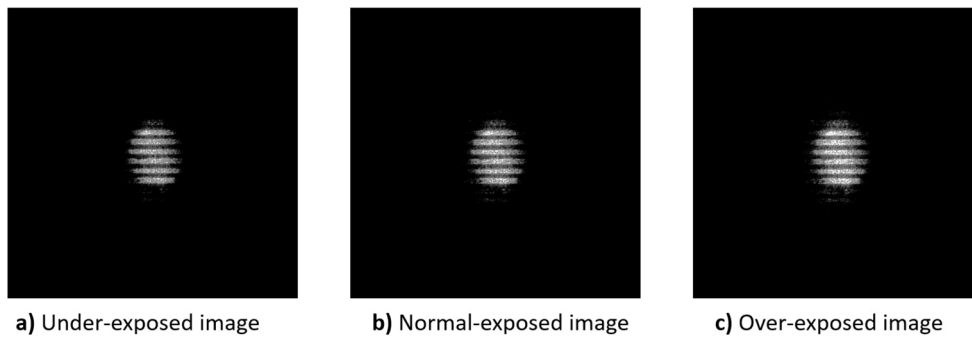


Fig. 4 Three images with different exposure levels

To characterize the initial normalized intensity flux distribution of the laser beam, the measurement is carried out on a white paper sheet (i.e.  $80\text{g.m}^{-2}$  of weight paper) instead of 3D printed samples, which serves as the output screen. This result will then be used as input for the numerical ray-tracing model. In the case of the measurement with the 3D printed samples, the laser is pointed on the top surface of the samples (according to the printing axis).

Through the use of the master curves illustrated in Fig. 6, it is possible to link the normalized energy received at a particular location in an image and the grayscale value of the pixel located at that position. For each sample, by dividing the normalized area energy ( $E$  in  $J.m^{-2}$ ) by the exposure time (using one of the three images) we obtain an intensity ( $I$  in  $W.m^{-2}$ ) flux distribution map at the weld interface (as illustrated in Fig. 5).

## Numerical section

### Generation of the microstructure

To describe the microstructure of the 3D printed part, a regular array of void grooves aligned in the direction of the filament is assumed in the numerical model. Idealized astroid-shaped and half astroid-shaped are considered to represent the void shapes for two typical sample types I and II

with  $e = 0.2\text{mm}$  and  $e = 0.3\text{mm}$  respectively. For each void configuration, a rectangular representative unit cell (RUC) containing a void at the center is created (see Fig. 7). The RUC is in the XZ plane following the coordinate system defined in the printing process, with the vertical Z-direction being the direction of laser beam projection. It is worth noting that, in the proposed numerical model, the laser is pointed from bottom to top. Therefore, in the case of sample type II, the peak of the half astroid-shaped is pointing downwards. The size of the voids is computed based on the measured porosity of the voids from experimental images (Fig. 2). The data used in this study are listed in Table 2.

Figure 8 shows the multi-scale mesh used to discretize the 3D printed parts for ray-tracing simulations. As can be seen from the figure, the first scale, the so-called macroscopic mesh, is a regular hexahedral mesh. Then, each macro-element is discretized by a periodic microscopic mesh. The 3D microscopic mesh is generated by extrusion of the 2D RUCs in the direction Y by a unit distance.

### Ray-tracing simulation

In order to describe the interaction between the laser beam and the 3D printed thermoplastic part, the ray-tracing method is chosen. This method has the advantage of following the laser beam propagation into a complex structure. In previous studies, the ray-tracing method has been successfully

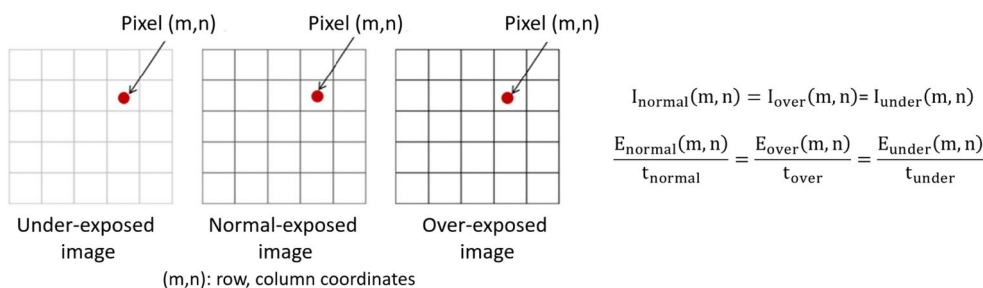


Fig. 5 Bracketing exposure representation.  $I_k$  and  $E_k$  stand respectively for intensity and area energy received in each pixel location (m,n), and  $t_k$  stands for exposure time;  $k = \{normal, over, under\}$

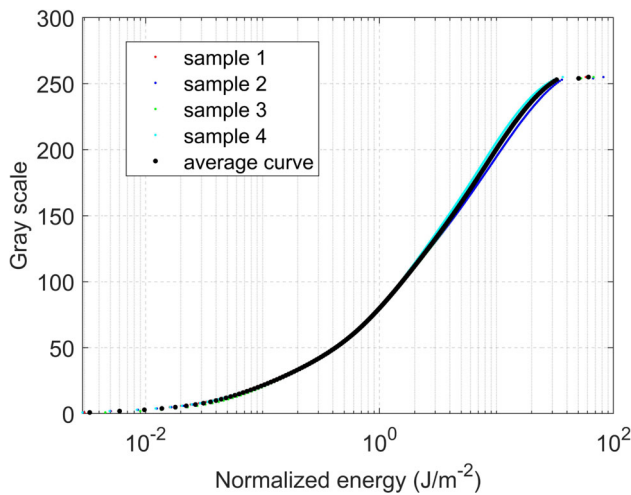


Fig. 6 Master curves for gray levels versus normalized light energy

employed to simulate the transmission of the laser beam through the continuous glass fiber reinforced thermoplastic composites [19, 20]. In this method, the laser beam is discretized into a set of rays, then the path of each ray is followed in the model geometry. This method is very close to the physics of light propagation since a ray can represent the path of a photon. Therefore, the ray-tracing method allows for taking into account the different optical effects (i.e. absorption, refraction) of light through the material. In the case of transparent 3D printed parts, the laser beam diffuses through the complex heterogeneous microstructure due to the numerous refractions occurring at the matrix/void interfaces.

The laser beam is represented by thousands of rays randomly distributed on a predefined incident surface. This predefined surface is chosen regarding the laser spot shape. In this application, it is an ellipse of major axis 4.0mm and minor axis 3.0mm. The major axis is perpendicular to the direction of the filament. The incident ray directions are defined from the bottom up and are perpendicular to the sample surface. The incident surface is assumed to be perfectly

flat. Thanks to this assumption, the diffraction of light due to surface roughness is negligible.

The power assigned to individual rays is determined by referring to the experimental data obtained from the measurement of the initial laser intensity profile in “Laser intensity profile measurement”. Thereby, an initial normalized power flux distribution map of the laser beam is established (see Fig. 11). Given that the power of the laser used is  $P_{laser} = 1mW$ , the initial power assigned to each ray is calculated by Eq. 1:

$$p_0(x, y) = \frac{P_{laser} \times p_{normalized}(x, y)}{\sum p_{normalized}(x, y)} \tag{1}$$

The path of each ray is first followed in the macroscopic mesh. In each macro element, the ray enters the microscopic mesh and then it is followed in the microelements. It is important to note that the computation of the intersection between a considered ray and all the micro mesh at the same time is obviously very time-consuming. The macroscopic mesh serves as a first filter before considering the interaction of the ray with the microscopic mesh. By this means, only one microscopic mesh is considered each time. As a result, this two-scale calculation allows for a significant reduction of computational cost.

The main phenomenon linked to the light scattering effect at the macroscopic scale is the multiple refractions in the structure at the microscopic scale. Refraction causes a change in the direction of light at the air-matrix interface. In the ray-tracing method, each time a ray encounters a change of medium, refraction is taken into account using the Snell-Descartes law:

$$n_1 \sin \theta_1 = n_2 \sin \theta_2 \tag{2}$$

where  $n_1, n_2$  are the refractive indices,  $\theta_1$  is the angle of the incident ray at the dioptré, and  $\theta_2$  is the angle of the refracted ray. Refractive indices of the polymer and the void

Fig. 7 Representative unit cell (RUC) for different void configurations. (a) fully astroid-shaped void for sample type I; (b) half astroid-shaped void for sample type II

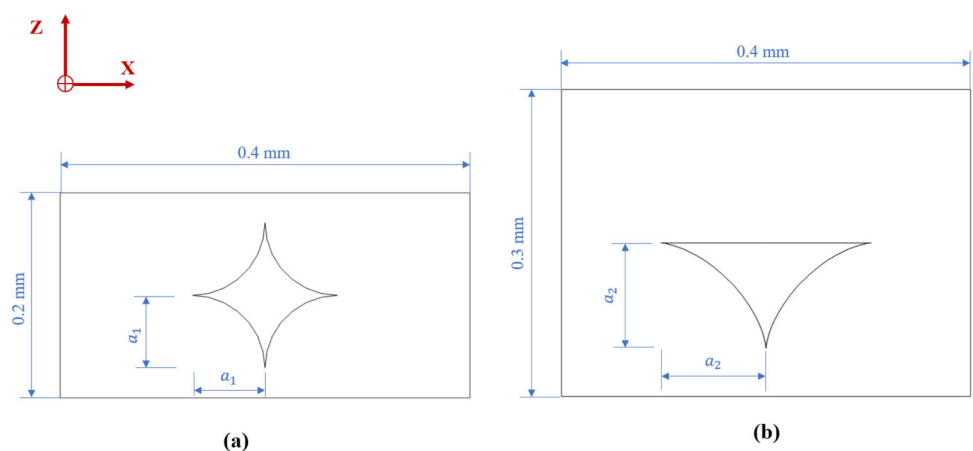


**Table 2** Size of the voids

Sample	Layer thickness	Porosity	Void size
Type I	0.2 mm	7.45 ± 0.2%	$a_1 = 0.071$
Type II	0.3 mm	5.23 ± 0.2%	$a_2 = 0.103$

are respectively  $n_m = 1.49$  and  $n_v = 1.00$ . The reflection of light at the dioptré is considered to be negligible in front of refraction [20]. Hence, partially reflected light is not taken into account in the calculation to lower the computation cost.

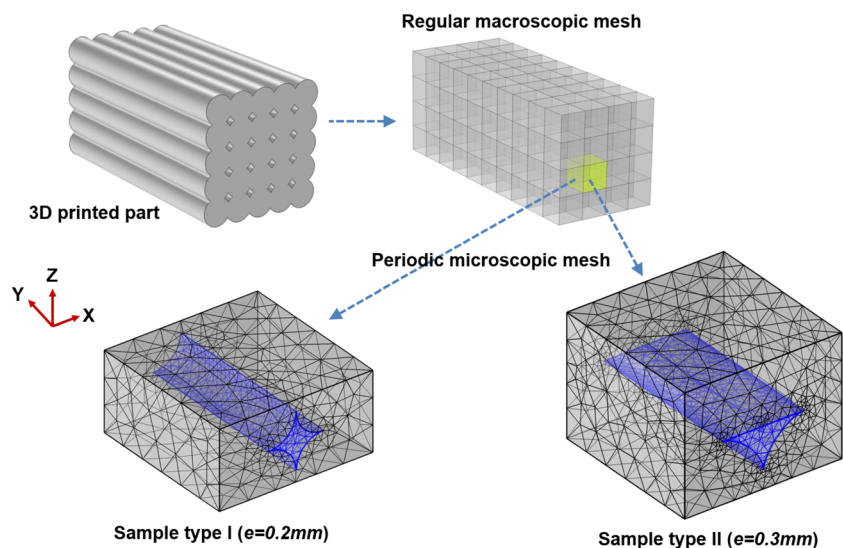
The attenuation of the ray power due to absorption within the media throughout the ray path is taken into account in the ray-tracing model by using the Beer-Lambert law. Following the real ray path, the final power assigned to each ray reaching the weld interface is calculated by Eq. 3:

$$p(l) = (1 - \rho)P_0e^{-K_h l} \tag{3}$$

where  $l$  represents the ray path length,  $\rho = 0.07$  [24] stands for the reflectivity at the incident surface.  $K_h$  is the homogenized absorption coefficient of the 3D printed thermoplastic part. It was demonstrated in Ref. [19] that the ratio between the average length of the path of rays in the air by the total average length path is equal to the void fraction. As a consequence, the homogenized absorption coefficient  $K_h$  can be computed using the rule of mixture. In this work,  $K_h$  is set equal to  $100m^{-1}$ .

Convergence of the model is performed during the calculations to find out the required number of rays. New rays are generated until the resulting total transmitted energy at the welding interface does not vary or when the error level becomes acceptable. As shown in Fig. 9,  $2 \times 10^5$  rays are sufficient for acquiring a good convergence for all simulations in this study.

**Fig. 8** Discretization of the 3D printed parts for ray-tracing simulation



### Thermal simulation

In order to show the influence of the scattering effect on the weld quality (i.e. heat affected zone), thermal simulations are performed using commercial FEM software COMSOL Multiphysic®. The numerical model is composed of two domains: a 3D printed transparent component made of PETG material, and an absorbent substrate of the same material, filled with black carbon. For the sake of simplicity, as a first step, the thermal properties of pure material are used (i.e. without homogenization) for both components, which are listed in Table 3. A perfect thermal contact is assumed at the interface between the two components. All the exposed surfaces are prescribed a convective heat flux boundary condition, with a heat transfer coefficient of  $h = 10[W/(m^2.K)]$  [24]. To quantify the effect of scattering on the temperature field, a first model (model 1), where scattering is neglected, is proposed. With model 1, the attenuation of the laser intensity due to absorption within the transparent part is modeled by using Eq. 4:

$$I(z) = (1 - \rho) \times \tau \times I_0 \times e^{-zD} \tag{4}$$

where  $I_0$  is the initial laser intensity coming from the laser,  $\tau$  is the transmissivity of the transparent part at the laser wavelength (i.e. the ratio of rays that reach the weld interface to the total number of rays),  $\rho$  is the reflectivity at the incident surface, and  $z$  is the sample thickness.  $D$  stands for the macroscopic extinction coefficient. It is noted that  $\tau$  and  $D$  can be obtained either by ray-tracing simulations or by experimental measurements using an IR spectrometer. In this work,  $\tau$  and  $D$  were obtained as results from ray-tracing simulations.

In the second model (model 2), the scattering effect is considered. For this model, the beam intensity profile, reaching the weld interface, calculated by ray-tracing simulations

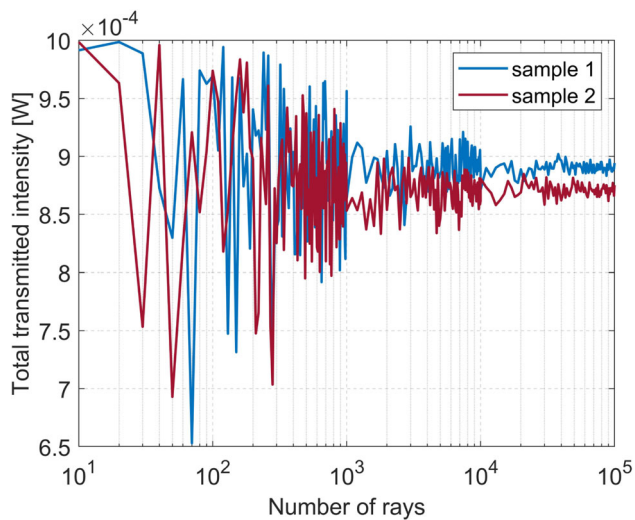


**Fig. 9** Convergence of number of rays

is applied as the boundary condition. Assuming that the absorbent substrate has an infinite absorption coefficient, the laser intensity is imposed on the weld interface as an inward heat flux to the absorbent part. The model geometry and mesh for the thermal simulation in COMSOL Multiphysic® can be seen in Fig. 10. The assembly dimensions are 40mm along the direction Y and 20mm along the direction X. In the direction Z, the assembly is sized of 4mm, so 2mm in thickness for each component. For moving laser source in the LTW process, scanning speed is also included in the model, therefore  $v_{laser} = 2 \text{ mm} \cdot \text{s}^{-1}$  along the direction Y.

## Results and discussion

### Confrontation between simulation and experiment

In this section, we use the intensity distribution maps at the weld interface obtained from the experimental procedure to validate the ray-tracing simulations.

Figure 11 shows the intensity distribution of the laser beam before and after passing through the sample. Obviously, the scattering of light within the sample causes a redistribution of the laser intensity, leading to the formation of small slits where the laser intensity is significantly reduced. These slits are formed at locations where there are void grooves in the

sample and are the result of the multiple refractions of the laser light at the air-matrix interfaces. In contrast, areas of the sample with no void grooves allow the laser light to travel along straight paths with no scattering. In addition, these areas also receive intensities from the scattered zones, resulting in concentrated areas of laser light. Overall, the laser beam behavior is influenced by the sample's microstructure and can result in complex intensity patterns that depend on the presence or absence of the void grooves. It can be also seen in Fig. 11e that the ray-tracing model effectively simulates this feature, resulting in an intensity map that closely matches the experimental one.

To achieve a more quantitative comparison, the laser beam profiles at the central lines of the weld interface in the directions perpendicular and parallel to the filament are plotted in Fig. 12. It is apparent from the figure that there is a good agreement between simulations and measurements. The redistribution of the laser intensity after passing through the sample is well reproduced by the numerical model. It can be observed in the linear scale (Fig. 12a) that the concentrated and attenuated areas of the laser intensity that were mentioned earlier are accurately predicted. In the logarithmic scale (Fig. 12b), the spread of the laser beam can be seen. One can readily observe that there is no spreading taking place in the direction parallel to the filament (Fig. 12d). This reflects that the scattering phenomenon is absent in this direction. This phenomenon has also been observed in the case of a unidirectional (UD) composite in previous work [20, 25].

The confrontations between simulation and experiment for other samples are presented in Fig. 13. It is shown that, in all cases, the intensity distributions in the central zone of the beam are well predicted since the profiles are very similar. In the logarithmic scale, the results show that the spread of the laser beam is fairly better predicted for the cases of sample type II compared with one of sample type I. For both cases of sample type I, there is a visible discrepancy in the region far from the beam center. This discrepancy can be attributed to the following. The voids are not perfectly astroid-shaped and have regular alignment, hence different than those used in the ray-tracing models. Similarly, the void shape in some regions of the sample type I might be quite small compared to the average void fraction used in the models (see Fig. 2).

### Influence of sample thickness

In this section, the influence of the sample thickness on the transmitted laser intensity is investigated. For the sake of clarity, the plots of simulated and experimental results are separated to achieve more accurate comparisons. The simulated results of the three samples with different thicknesses are shown together in Fig. 14a, and the experimental ones are shown in Fig. 14b. From the figure, the attenuation of laser

**Table 3** Thermal properties of PETG

Properties	Value
Density ( $\rho$ )	1250 [kg/m <sup>3</sup> ]
Specific heat capacity ( $C_p$ )	1800 [J/(kg.K)]
Thermal conductivity ( $k$ )	0.2 [W/(m.K)]



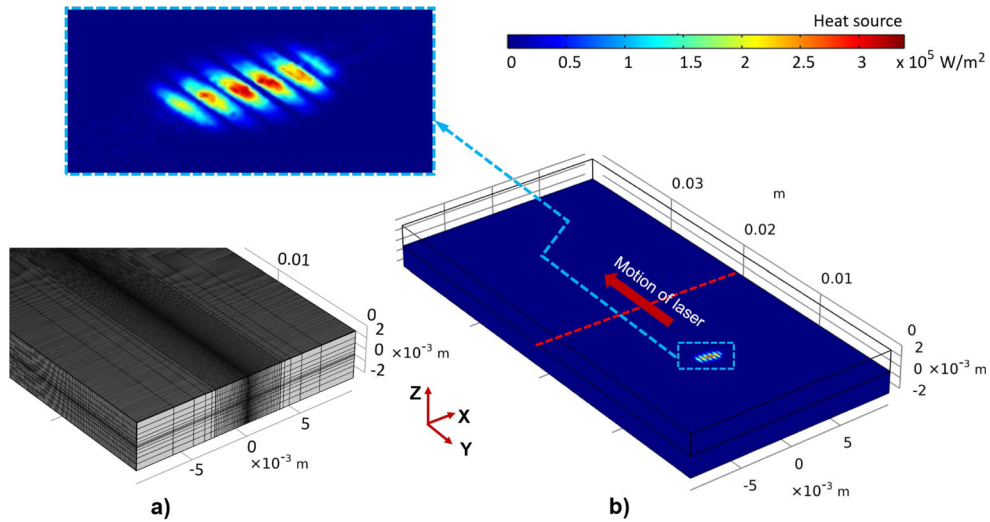


**Fig. 10** (a) 3D mesh of the two sample's parts in COMSOL Multiphysics (b) Numerical model geometry with a surface heat source for thermal simulations

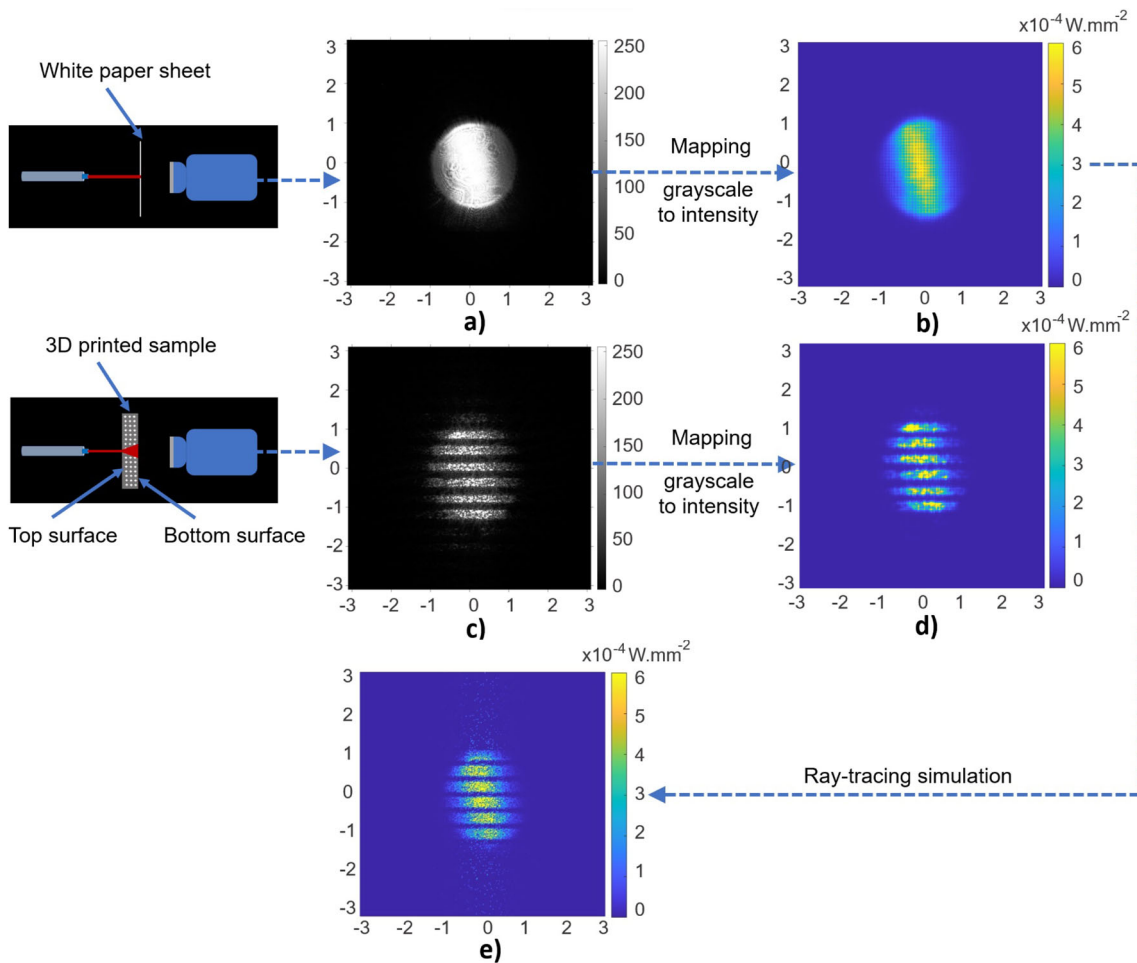


**Fig. 11** Initial laser beam profile and intensity distribution map at the weld interface of the samples. (a) Experimental grayscale image of the laser beam; (b) Initial intensity distribution map of the laser beam; (c) Experimental grayscale image of the sample type I - 2mm; (d) Experimental intensity distribution map of the sample type I - 2mm; (e) Numerical intensity distribution map of the sample type I - 2mm

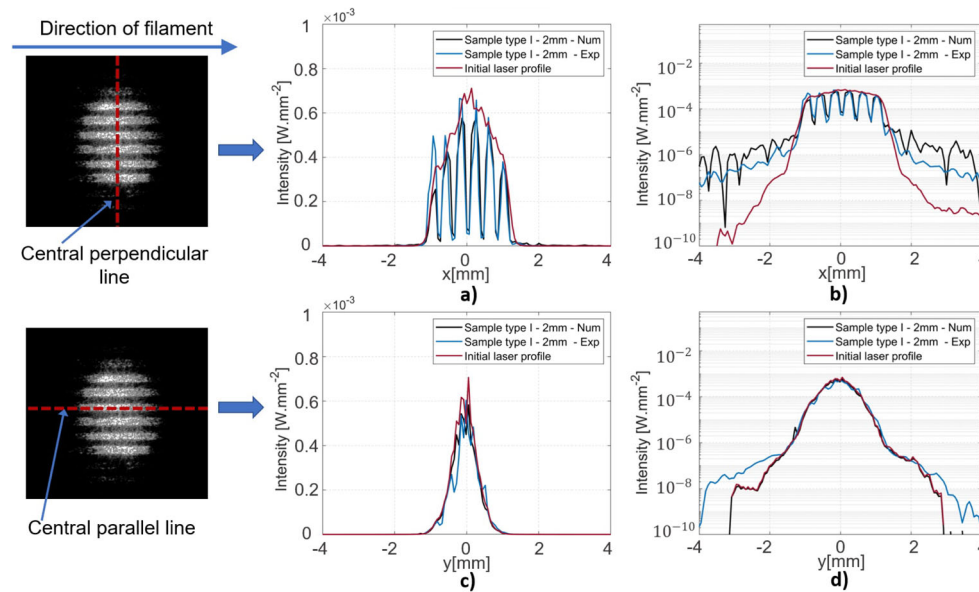


**Fig. 12** Laser beam profile at the central lines of the weld interface in the direction perpendicular to the filament: a) linear scale, b) logarithmic scale; and in the direction of the filament: c) linear scale, d) logarithmic scale

beam intensity with the increase in sample thickness can be clearly observed, particularly in the central area of the laser.

### Influence of void shape

The influence of the void shape on the intensity distribution map of the laser beam at the weld interface is shown in Fig. 15. It is observed that the size of the slits, where the laser intensity is reduced, is a function of the void size. As a result, the ones observed in sample type II are slightly larger than in sample type I. Accordingly, for sample type II, the light intensity in concentrated areas reaches higher peaks. (see Fig. 15b).

In order to compare the light scattering level inside the two sample types, the empirical cumulative distribution functions of the ray path length are depicted in Fig. 16a. It is important to note that, rays whose path lengths are lower than the thickness of the samples, are exited the numerical geometry through other faces than the weld interface (i.e. sides, and top faces). Thus, the quantity of these rays might represent the light scattering level within the samples. Accordingly, the probabilities of these rays are 0.07 and 0.11 for sample type I (2mm) and sample type II (2.1mm) respectively. For thicker samples, these probabilities also increase, namely 0.09 and 0.17 for sample type I (4mm) and sample type II (3.9mm) respectively. From this analysis, it can be concluded that the light scattering level inside sample type II is slightly higher compared to sample type I. Also, the light scattering level increases with the thickness of the sample. Figure 16b shows the total transmitted power (i.e. the integral on the surface) received at the weld interface as a function of the sample thickness for two sample types. As a result, samples type

I allow more light to pass through than type II. It can also be seen that the greater the sample thickness, the lower the energy reaching the welding interface. From this result, the macroscopic extinction coefficient of the laser intensity  $D$  can be calculated according to the Beer-Lambert law (Eq. 5):

$$I(z) = I_0 \times e^{-zD} \quad (5)$$

where  $I_0$  is the initial laser intensity coming from the laser device, before entering the sample, and  $z$  is the sample thickness. The macroscopic extinction coefficient  $D$  is given by the calculation of the slope of the line  $\ln(I(z))$  vs.  $z$  as can be shown in Fig. 16c. Accordingly, the computed results are respectively  $D = 113.7m^{-1}$  and  $D = 123.3m^{-1}$  for sample type I and sample type II.

### Influence of the scattering effect on the weld quality

For the sake of comparison, thermal simulations are performed for two different types of samples with a thickness of 2mm. In this application, to achieve a welding temperature at the interface (i.e. above the glass transition temperature  $T_g = 81^\circ C$ ), the intensity of the laser is magnified 500 times. The maximum temperature profiles achieved on a line perpendicular to the weld seam (i.e. the red dotted line in Fig. 10b) are shown in Fig. 17. Compared with the no-scattering simulation, the scattering effect results in the formation of narrowed regions along the weld seam where the temperature is significantly reduced. This confirms that the thermal diffusion rate is insufficient to compensate for the non-homogenization of the intensity distribution due to the

**Fig. 13** Comparison of simulation results and measurement results (a) Samples type I - 4mm; (b) Samples type I - 8mm; (c) Samples type II - 2.1mm; (d) Samples type II - 3.9mm

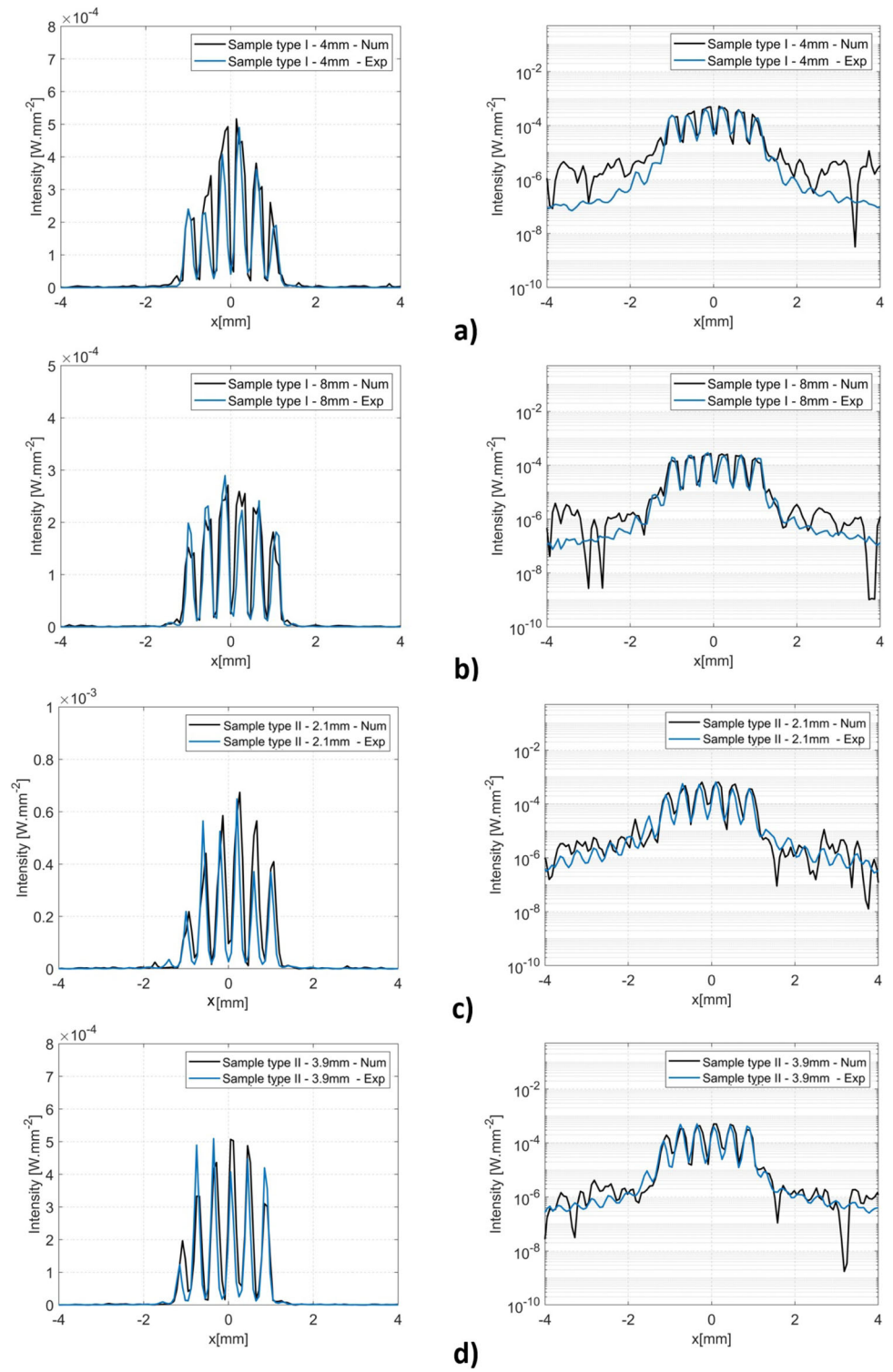


**Fig. 14** (a) Numerical and (b) experimental results for three samples with different thicknesses

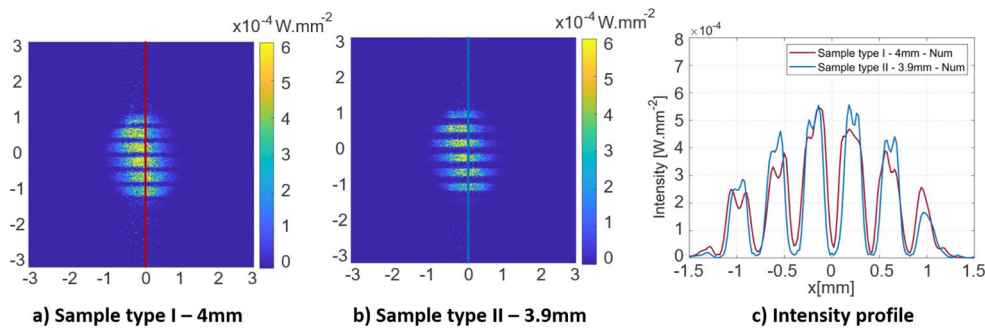
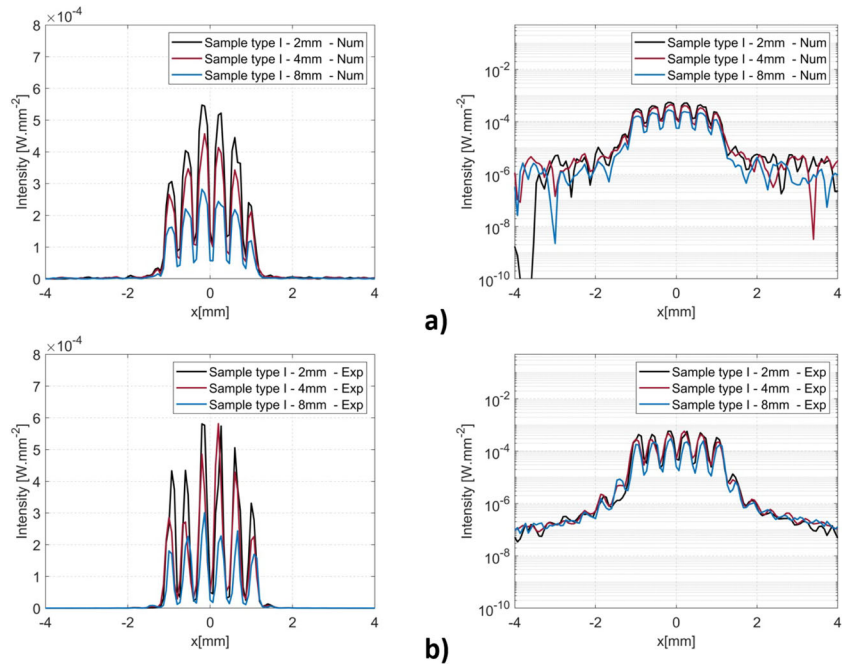


**Fig. 15** Comparison of laser intensity map for two different sample types. Red line (a) and cyan line (b) represent central perpendicular lines, their intensity profiles are plotted in (c)

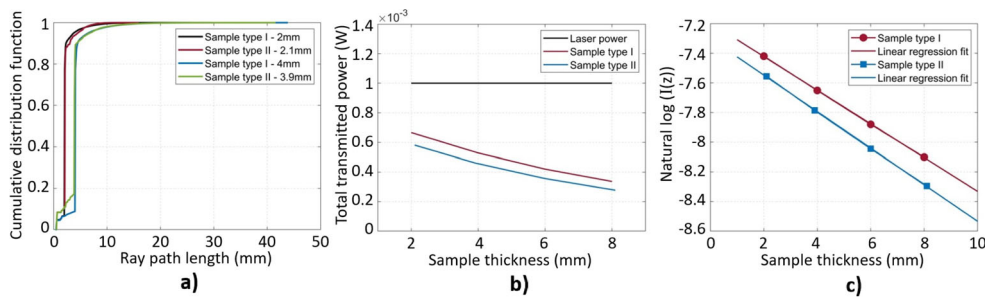


**Fig. 16** Comparison results for two different sample types. (a) Cumulative distribution function of the ray length path; (b) Total transmitted power  $I(z)$  vs. sample thickness; (c) Computation of the macroscopic extinction coefficient  $D$

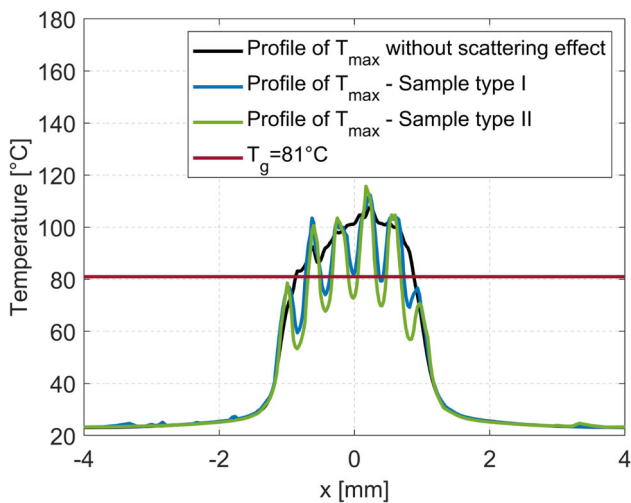


**Fig. 17** Comparison of simulated maximum temperature profiles

scattering effect. The above-mentioned regions either lack the required temperature for welding or produce unsatisfactory welds. Consequently, the weld quality along the seam line width is seriously impacted. It can also be seen that this adverse effect is more straightforward in the case of sample type II compared to sample type I.

## Conclusion

The inherent layer-by-layer production of 3D printing technology results in a complex heterogeneous microstructure with a larger amount of porosity inside the printed parts. Consequently, the laser intensity is subjected to the scattering phenomenon when it propagates through the thickness of the 3D printed component during the LTW process. Obviously, comprehension of the light scattering effect allows controlling the interface weld temperature for achieving a high-quality assembly.

In this study, we have carried out the influence of 3D printing process parameters on the microstructure (i.e. void shape and size) of the 3D printed thermoplastic parts. Subsequently, two typical void morphology of the 3D printed parts were investigated to examine the light scattering effect.

We have presented a ray-tracing model, which is able to simulate both light absorption and light scattering phenomena during the transmission of laser intensity through a semi-transparent and diffusive media. The proposed model was able to predict effectively the intensity distribution map of the laser beam reaching the weld interface. In addition, it allowed for taking into account the differences in the microstructure of different sample types. The influence of the material thickness was also investigated, which demonstrated the growing impact of the light scattering effect as the material thickness increases. The reliability of the numerical

model was validated by experimental measurements that used a laser as a light source and a reflex camera as a measuring device. In order to assess the influence of the scattering effect on the quality of the weld, 3D thermal simulations were conducted, which allowed for predicting the temperature field during the LTW process. The results showed a marked reduction in the quality of the weld due to the scattering effect.

Future work will aim to further extend the applications of the model to predict the influence of filling patterns on the light scattering of the laser beam within the 3D printed parts. Consequently, the ray-tracing model will be coupled to a FEM model to simulate the temperature field during the LTW process of 3D printed CCFRCs.

**Acknowledgements** The authors extend their sincere appreciation to the National French Research Agency's ANR JCJC program for funding the SHORYUKEN project (Grant agreement n° ANR-21-CE10-0007-01) through the AAPG 2021-CE10 "Industrie et Usine du Futur: Homme, Organisation, Technologies" initiative. Without their support, this work would not have been possible.

## Declarations

**Conflict of Interests** The authors declare no conflict of interest.

## References

- Kabir SMF, Mathur K, Seyam A-FM (2020) A critical review on 3D printed continuous fiber-reinforced composites: History, mechanism, materials and properties. *Composite Structures* 232:111476. <https://doi.org/10.1016/j.compstruct.2019.111476>. Accessed 19 Oct 2022
- Le A-D, Cosson B, Asséko ACA (2021) Simulation of large-scale additive manufacturing process with a single-phase level set method: a process parameters study. *The Int J Adv Manuf Technol* 113(11):3343–3360. <https://doi.org/10.1007/s00170-021-06703-5>. Accessed 27 July 2022
- Werken N, Tekinalp H, Khanbolouki P, Ozcan S, Williams A, Tehrani M (2020) Additively manufactured carbon fiber-reinforced composites: State of the art and perspective. *Additive Manufacturing* 31:100962. <https://doi.org/10.1016/j.addma.2019.100962>. Accessed 12 April 2022
- Chacón JM, Caminero MA, García-Plaza E, Núñez PJ (2017) Additive manufacturing of PLA structures using fused deposition modelling: Effect of process parameters on mechanical properties and their optimal selection. *Materials & Design* 124:143–157. <https://doi.org/10.1016/j.matdes.2017.03.065>. Accessed 21 Sept 2022
- Tian X, Liu T, Yang C, Wang Q, Li D (2016) Interface and performance of 3D printed continuous carbon fiber reinforced PLA composites. *Compos A: Appl Sci Manuf* 88:198–205. <https://doi.org/10.1016/j.compositesa.2016.05.032>. Accessed 28 April 2022
- Zhang Z, Yavas D, Liu Q, Wu D (2021) Effect of build orientation and raster pattern on the fracture behavior of carbon fiber reinforced polymer composites fabricated by additive manufacturing. *Additive Manufacturing* 47:102204. <https://doi.org/10.1016/j.addma.2021.102204>. Accessed 12 April 2022

7. Berger S, Oefele F, Schmidt M (2015) Laser transmission welding of carbon fiber reinforced thermoplastic using filler material-A fundamental study. *Journal of Laser Applications* 27(S2):29009. <https://doi.org/10.2351/1.4906391>. Publisher: Laser Institute of America. Accessed 28 Feb 2023
8. Akué Asséko AC, Cosson B, Schmidt F, Le Maout Y, Gilblas R, Lafranche E (2015) Laser transmission welding of composites - Part B: Experimental validation of numerical model. *Infrared Physics & Technology* 73:304–311. <https://doi.org/10.1016/j.infrared.2015.10.005>
9. Chabert F, Garnier C, Sangleboeuf J, Akue Asseko AC, Cosson B (2020) Transmission laser welding of polyamides: effect of process parameter and material properties on the weld strength. *Procedia Manufacturing* 47:962–968. <https://doi.org/10.1016/j.promfg.2020.04.297>
10. Le A-D, Akué Asséko AC, Nguyen T-H-X, Cosson B (2023) Laser intensity and surface distribution identification at weld interface during laser transmission welding of thermoplastic polymers: A combined numerical inverse method and experimental temperature measurement approach. *Polymer Engineering & Science*. <https://doi.org/10.1002/pen.26405>
11. Ilie M, Kneip J-C, Mattei S, Nichici A, Roze C, Girasole T (2007) Laser beam scattering effects in non-absorbent inhomogeneous polymers. *Optics Lasers Eng* 45(3):405–412. <https://doi.org/10.1016/j.optlaseng.2006.07.004>. Accessed 05 June 2023
12. Akué Asséko AC, Cosson B, Deleglise M, Schmidt F, Le Maout Y, Lafranche E (2015) Analytical and numerical modeling of light scattering in composite transmission laser welding process. *Int J Mater Form* 8(1):127–135. <https://doi.org/10.1007/s12289-013-1154-7>
13. Chen M, Zak G, Bates PJ (2013) Description of transmitted energy during laser transmission welding of polymers. *Welding in the World* 57(2):171–178. <https://doi.org/10.1007/s40194-012-0003-5>. Accessed 20 July 2022
14. Xu XF, Parkinson A, Bates PJ, Zak G (2015) Effect of part thickness, glass fiber and crystallinity on light scattering during laser transmission welding of thermoplastics. *Optics & Laser Technology* 75:123–131. <https://doi.org/10.1016/j.optlastec.2015.06.026>. Accessed 09 May 2022
15. Zak G, Mayboudi L, Chen M, Bates PJ, Birk M (2010) Weld line transverse energy density distribution measurement in laser transmission welding of thermoplastics. *J Mater Process Technol* 210(1):24–31. <https://doi.org/10.1016/j.jmatprotec.2009.08.025>. Accessed 09 May 2022
16. Kuklik J, Mente T, Wippo V, Jaeschke P, Kaielerle S, Overmeyer L (2022) Enabling laser transmission welding of additively manufactured thermoplastic parts using an expert system based on neural networks. *Journal of Laser Applications* 34(4):042022. <https://doi.org/10.2351/7.0000787>. Publisher: Laser Institute of America. Accessed 25 Oct 2022
17. Kuklik J, Mente T, Wippo V, Jaeschke P, Kuester B, Stonis M, Kaielerle S, Overmeyer L (2022) Laser welding of additively manufactured thermoplastic components assisted by a neural network-based expert system, vol 11994, pp 119–124. SPIE. <https://doi.org/10.1117/12.2609365>
18. Cosson B, Akué Asséko AC, Dauphin M (2018) A non-destructive optical experimental method to predict extinction coefficient of glass fibre-reinforced thermoplastic composites. *Optics & Laser Technology* 106:215–221. <https://doi.org/10.1016/j.optlastec.2018.04.009>. Accessed 09 Mar 2022
19. Cosson B, Akué Asséko AC, Lagardère M, Dauphin M (2019) 3D modeling of thermoplastic composites laser welding process - A ray tracing method coupled with finite element method. *Optics & Laser Technology* 119:105585. <https://doi.org/10.1016/j.optlastec.2019.105585>. Accessed 18 May 2022
20. Cosson B, Deléglise M, Knapp W (2015) Numerical analysis of thermoplastic composites laser welding using ray tracing method. *Composites Part B: Engineering* 68:85–91. <https://doi.org/10.1016/j.compositesb.2014.08.028>. Accessed 18 May 2022
21. Gao X, Qi S, Kuang X, Su Y, Li J, Wang D (2021) Fused filament fabrication of polymer materials: A review of interlayer bond. *Additive Manufacturing* 37:101658. <https://doi.org/10.1016/j.addma.2020.101658>. Accessed 13 May 2022
22. Gao X, Qi S, Zhang D, Su Y, Wang D (2020) The role of poly (ethylene glycol) on crystallization, interlayer bond and mechanical performance of polylactide parts fabricated by fused filament fabrication. *Additive Manufacturing* 35:101414. <https://doi.org/10.1016/j.addma.2020.101414>. Accessed 13-05-2022
23. Ghorbani J, Koirala P, Shen Y-L, Tehrani M (2022) Eliminating voids and reducing mechanical anisotropy in fused filament fabrication parts by adjusting the filament extrusion rate. *J Manuf Process* 80:651–658. <https://doi.org/10.1016/j.jmapro.2022.06.026>. Accessed 28 June 2022
24. Le A-D, Gilblas R, Lucin V, Maout YL, Schmidt F (2022) Infrared heating modeling of recycled PET preforms in injection stretch blow molding process. *Int J Therm Sci* 181:107762. <https://doi.org/10.1016/j.ijthermalsci.2022.107762>. Accessed 28 Feb 2023
25. An Y, Myung JH, Yoon J, Yu W-R (2022) Three-dimensional printing of continuous carbon fiber-reinforced polymer composites via in-situ pin-assisted melt impregnation. *Additive Manufacturing* 55:102860. <https://doi.org/10.1016/j.addma.2022.102860>. Accessed 13 May 2022

**Publisher's Note** Springer Nature remains neutral with regard to jurisdictional claims in published maps and institutional affiliations.

Springer Nature or its licensor (e.g. a society or other partner) holds exclusive rights to this article under a publishing agreement with the author(s) or other rightsholder(s); author self-archiving of the accepted manuscript version of this article is solely governed by the terms of such publishing agreement and applicable law.